Influence of Crystalline Nanoprecipitates on Shear-Band Propagation in Cu-Zr-Based Metallic Glasses

Tobias Brink,[1,*] Martin Peterlechner,[2] Harald Rösner,[2] Karsten Albe,[1] and Gerhard Wilde[2]

[1]*Fachgebiet Materialmodellierung, Institut für Materialwissenschaft, Technische Universität Darmstadt, Jovanka-Bontschits-Straße 2, D-64287 Darmstadt, Germany*
[2]*Institut für Materialphysik, Westfälische Wilhelms-Universität Münster, Wilhelm-Klemm-Straße 10, D-48149 Münster, Germany*

The interaction of shear bands with crystalline nanoprecipitates in Cu-Zr-based metallic glasses is investigated by a combination of high-resolution TEM imaging and molecular-dynamics computer simulations. Our results reveal different interaction mechanisms: Shear bands can dissolve precipitates, can wrap around crystalline obstacles, or can be blocked depending on the size and density of the precipitates. If the crystalline phase has a low yield strength, we also observe slip transfer through the precipitate. Based on the computational results and experimental findings, a qualitative mechanism map is proposed that categorizes the various processes as a function of the critical stress for dislocation nucleation, precipitate size, and distance.

I. INTRODUCTION

Metallic glasses (MGs) have advantageous mechanical properties, such as a high yield strength and a large elastic limit, but suffer from brittle failure, especially under tension, at temperatures significantly below the glass transition [1,2]. Under compression, improved ductility is found for composites of MGs and crystalline secondary phases, namely, for Cu-Zr-based [3–7], Cu-Ti-based [8], and Zr-Ti-based MGs [9–11]. Under tension, a small ductility with 1%–2% strain is observed for Cu-Zr composites containing nanocrystals [12–14]. With a higher volume fraction of the crystalline phase, not only compressive but also significant tensile ductility is reported for Zr-Ti-based [11,15], Ti-based [16], and Cu-Zr-based MGs [17,18].

For dendritic precipitates, there is a correlation between the location of dendrites and the occurrence of shear-band patterns [9,10]. The improved ductility is generally ascribed to the increased number of shear bands and their limited length given by the constraints of the crystalline phase [11]. Thus, a high volume fraction of ductile crystalline phase improves the ductility in compression and microindentation tests, while a brittle secondary phase does not [19]. This is confirmed by Song *et al.,* who suggest a crystalline volume fraction between 40% and 80% in Cu-Zr-based MGs for obtaining good mechanical properties [20], which is consistent with the fact that tensile

ductility is observed only in glasses with high volume fractions of ductile crystalline phases [11,16–18].

While the enhancement of macroscopic ductility of MGs with high volume fractions of a ductile crystalline phase can be explained by simple composite models, the influence of nanoprecipitates on the mechanical properties of MGs containing a much lower volume fraction of crystalline matter is still not clear. Similar to the case of dendritic precipitates, shear-band patterns are also observed in glasses containing small spherical crystallites with sizes around 2 nm [5]. These nanoprecipitates can grow during deformation in certain metallic glasses [4,6,12–14,21]. An increased growth rate of nanocrystallites in shear bands is observed [22], which has been related to enhanced atomic mobility inside shear bands [23,24]. Deformation-grown nanocrystallites are observed to contain twins [12,14,21], which occur only in larger crystallites, e.g., with a size greater than 20 nm in a Cu-Zr-Al MG [14]. These deformation-grown precipitates are the possible reason for strain hardening during nanoindentation [6] as well as increased plastic strain during compression [4]. It is proposed that the participation of the crystallites in the plastic deformation is the reason for the enhanced ductility: Wu *et al.* demonstrate that reducing the stacking-fault energy of $B2$ CuZr by alloying leads to increased twinning and higher ductility under tension [25]. Pauly *et al.* propose that a martensitic transformation from the $B2$ phase to the $B19'$ phase with a subsequent volume change is responsible for toughening in Cu-Zr-based metallic glasses [12]. This interpretation, however, is not generally accepted. Corteen, Rainforth, and Todd, in contrast, note that the volume change of the martensitic transformation is very small and cannot contribute significantly to toughening [26]. They instead suggest that precipitates increase plasticity by

*brink@mm.tu-darmstadt.de

favoring the nucleation of new shear bands over the growth of critical shear bands. Indeed, recent simulation and experimental results provide evidence for the fact that crystal-glass interfaces serve as nucleation sites for shear bands and are therefore responsible for the simultaneous nucleation of multiple shear bands [27–29]. In tensile tests and corresponding molecular-dynamics (MD) simulations of nanolaminates of copper nanocrystals separated by thin Cu-Zr glass layers, the crystal-glass interface acts as a source or sink for dislocations. Shear transformation zones are activated by interactions with dislocations [30–32].

Computational studies on the interaction of crystalline precipitates with shear bands provide further insights into nanoscale mechanisms. Lund and Schuh conduct quasi-2D molecular-statics simulations of a binary Lennard-Jones system with a nanocrystal inclusion [33]. They identify three mechanisms of deformation, depending on the ratio of shear-band thickness to crystal size. For small crystals, the deformation is accommodated either in the interface (for example, by rotation) or by dissolution of the crystal. For wide shear bands and intermediate crystal sizes, dislocations in the crystal nucleate at the interface. Finally, for crystals larger than the shear band, they observe homogeneous dislocation nucleation due to stress building in the nanocrystal center. However, it is somewhat unclear how the observed homogeneous dislocation nucleation depends on the artificially induced shear band and the resulting stress state in the system. Shi and Falk conduct molecular-dynamics simulations on a monatomic amorphous model system with a high fraction of bcc nanocrystallites [34]. They find that deformation is induced at the interfaces and that shear bands bend around crystallites away from a direction of maximum resolved shear stress. They also observe blocking of shear bands by crystallites. Because of the high fraction of crystalline phase, the system more closely resembles a nanocrystalline structure. The observation of the initiation of plastic deformation at interfaces still matches the simulations by Albe, Ritter, and Şopu [27] and underlines the importance of the crystal-glass interface in these composite systems.

While it has been shown that interfaces promote shear-band nucleation and that precipitates can act as obstacles or can deform together with the matrix, there is no comprehensive study that investigates the influence of the size and number density of the precipitates. Furthermore, some mechanisms governing the interaction between a propagating shear band and a preexisting precipitate have been observed but not investigated and discussed in detail. Therefore, the goal of this study is to investigate the interaction of a shear band with preexisting precipitates in Cu-Zr-based MGs. In the experimental part of the study, we anneal Zr-Cu-Ag-Al melt-spun ribbons to induce the formation of nanocrystalline precipitates. We present transmission electron microscopy (TEM) images of the samples before and after deformation by cold rolling and identify the effects of crystalline precipitates on the shear-band

propagation. Using molecular-dynamics computer simulations, we model composite systems with a metallic-glass matrix and crystalline precipitates. We control the initiation of a shear band using a stress concentrator and put precipitates in its propagation path. The focus of the simulations is on the size effects of "hard" precipitates that do not partake in the plastic deformation. Additionally, we study the shear-band interaction with "soft," plastically deformable precipitates. Finally, we derive a deformation map from the combined observations of simulations and experiments that classifies the observed mechanisms.

II. EXPERIMENT

A. Experimental setup

We prepare metallic-glass samples of nominal composition $Zr_{53.8}Cu_{31.6}Ag_{7.0}Al_{7.6}$ from pure components (Cu, 99.999%; Zr, 99.998%; Ag, 99.999%; Al, 99.999%; all in at. %) by prealloying using arc melting. After repeated arc melting with intermittent turning of the specimen to enhance homogenization, the entire ingots are inserted into quartz-glass crucibles for melt spinning. The weight loss during alloying is minimal, and subsequent composition analyses by energy-dispersive x-ray diffraction confirm that the composition of the material is equal to the nominal composition within the accuracy of the measurement. For melt spinning, the ingots are inductively melted under an Ar atmosphere, and the melt is ejected onto a rotating Cu wheel (tangential wheel velocity 30 m/s), resulting in completely amorphous thin ribbon samples of approximately 80-μm thickness. X-ray diffraction on the as-quenched ribbon samples does not indicate the presence of any crystalline fraction exceeding the sensitivity threshold of this method. Parts of the ribbon samples are cut to perform differential scanning calorimetry (DSC) measurements in a Perkin Elmer Diamond DSC device. Both isochronal and isothermal measurements under a purified Ar gas flow are conducted, and in conjunction with microstructure analyses the time and temperature dependence of the evolving crystalline fraction is determined. On the basis of these results, the samples for deformation processing are annealed in the DSC device at 410 °C for 3 h. This thermal treatment results in the formation of nanocrystalline precipitates with an average diameter of about 70 nm and a number density on the order of 10^{20} m^{-3}. The resulting microstructure is shown in Fig. 1. Given that the width of shear bands is on the order of 10 nm [35], there is no straight path for propagating shear bands to avoid the interaction with nanoprecipitates in these samples.

After the DSC heat treatment, the partially crystalline material is deformed by cold rolling at room temperature in one step to true strain values of about $\varepsilon = 5\%$ at room temperature, applying a strain rate of the order of $\dot{\varepsilon} = 1$ s^{-1}. Subsequently, specimens for TEM investigations are prepared by grinding, dimpling, and finally precision ion polishing (PIPS, Gatan), using a low acceleration voltage of 2.5 kV and low incidence
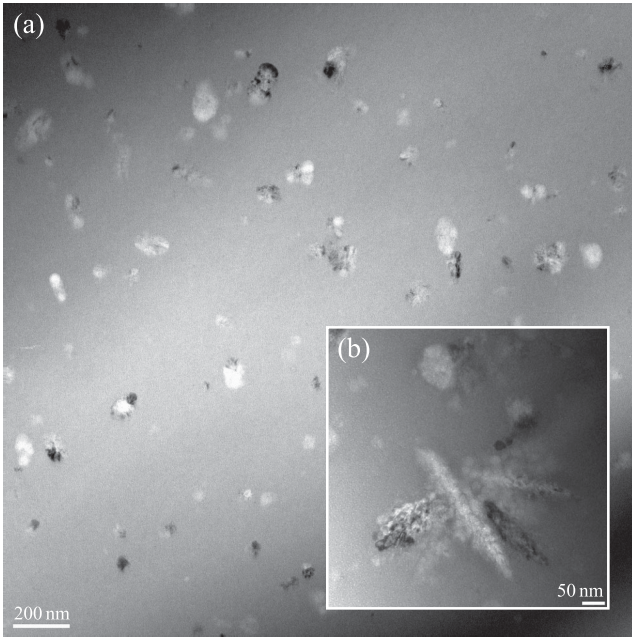
FIG. 1. An undeformed $Zr_{53.8}Cu_{31.6}Ag_{7.0}Al_{7.6}$ sample after annealing in a TEM bright-field image. An overview of the sample is shown in (a), with clearly visible crystalline precipitates. The inset (b) shows a magnified view, indicating the transition from globular to dendritic morphologies during precipitate growth. The different brightness of parts of one precipitate in (b) is most likely due to the different geometrical orientations of different parts of the same precipitate with respect to the incident electron beam. The strong black-white contrast change observed for some nano-crystals in (a) is most likely due to twinning.

angles ($< 4°$) to minimize damage by the preparation process. The electron transparent samples are then analyzed in dark-field, bright-field, and high-resolution transmission electron microscopy modes in a Zeiss Libra 200FE TEM operated at an acceleration voltage of 200 kV. Since intrinsic shear bands formed upon cold rolling could not be found during the TEM inspections of the thin foil regions, the shear bands generated as a result of sample preparation and/or subsequent sample manipulation are studied instead. Thus, the final sample state resembles the state in an *in situ* TEM experiment comparable to the work in Ref. [23], where the shear bands are generated at crack tips in the thin TEM foil.

B. Experimental results

Figure 2 shows a shear band in a sample after TEM preparation. It is noticeable that the shear band switches propagation directions in the vicinity of precipitates. Between precipitates 2 and 3, the shear band has an additional bend. The propagation path, in general, suggests that the shear band is "attracted" to the precipitates, possibly due to a stress field resulting from the density change on crystallization, which explains the change of direction between precipitates 2 and 3. Because of the processing of the
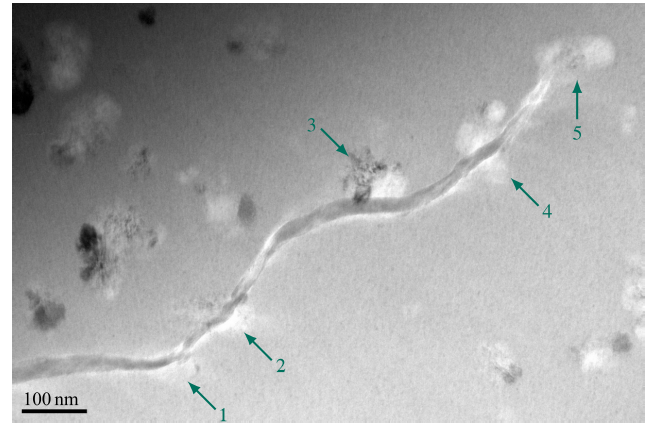

FIG. 2. TEM image of a shear band in a Zr-Cu-Ag-Al ribbon after deformation. The green arrows mark the positions of crystalline precipitates.

samples, it can be excluded that the repeated bending of the shear band results from a change of the external stress state: The deformation by cold rolling is performed in a single step, and the observed shear bands are created during TEM preparation, resembling an *in situ* experiment. As the path change in the presence of precipitates is rather large (in Fig. 2, around 45°) and correlated to the position of the precipitates, it is most likely induced by the presence of the precipitates. The literature supports this, as shear bands in homogeneous metallic glasses (Cu-Zr-based or otherwise) are straight on the length scale presented here [35–38]. It is therefore clear that the precipitates play a major role in influencing shear-band propagation and thereby the macroscopic plastic deformation of the material. TEM images of a second shear band, shown in Fig. 3, shed more light on this interaction. The shear band interacts with two precipitates: A crack follows the path of the shear band up to the first precipitate, and the shear band continues from the first to the second precipitate. Because of the visible crack opening near the first precipitate, it can be ruled out that the shear band originates from the second precipitate. While the first precipitate is passed, the second precipitate, which is encountered centrally, stops the shear band. This can also be observed at the end of the shear band in Fig. 2. A detailed analysis of the gray-scale intensity distribution of the high-resolution TEM (HRTEM) image in Fig. 3(e) indicates that the shear band changes its path slightly near the crystalline precipitate but does not proceed further or shows slip transfer into the precipitate. Additionally, a smaller, shear-band-like region emerges almost perpendicular to the previous propagation direction (yellow arrow). This indicates either a shear-band deflection or a nucleation of a new, perpendicular shear band. Based on the highly local nature of the intensity distribution and based on the comparison of the contrast of other precipitates, preparation artifacts can be excluded. Thus, this type of interaction observed here is part of the intrinsic interaction mechanism between precipitates and advancing shear bands.
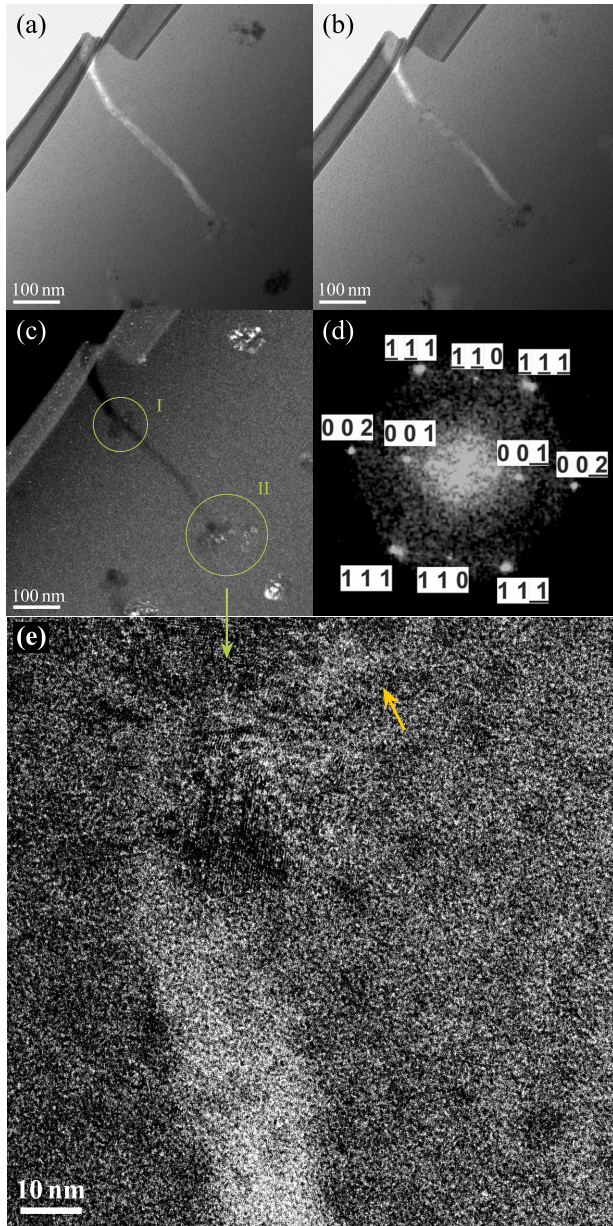
FIG. 3.   TEM and HRTEM images of a shear band. In the upper left corner, the electron transparent hole is visible, which stems from the sample preparation for TEM. (a), (b) Bright-field images of the same area, using a different tilt angle. The shear band appears as a white stripe, with part of it already cracked (bright white). (c) Dark-field image of the same area: The nanoprecipitates are visible and marked by circles. The crack stops at precipitate I; the shear band continues from there to precipitate II. (d) The power spectrum of precipitate II along the $\langle \bar{1}10 \rangle$ zone axis revealing superlattice reflections of the martensitic $B19'$ structure. (e) HRTEM image of precipitate II, showing the shear band stopping at the precipitate. The contrast in (c) and (e) is enhanced to improve the visibility of the precipitates and the shear band.

The power spectrum in Fig. 3(d) indicates a precipitate with $B19'$ crystal structure [39], which is consistent with prior observations in Cu-Zr-based MGs [12].

It is clear that the interaction of a propagating shear band with a distribution of crystalline precipitates depends on the actual stress state near the shear-band tip, the already accommodated stress by the shear-band propagation, and the details of the local distribution of crystalline precipitates, their sizes, and the residual stresses in the glass matrix due to the formation of the precipitates. Depending on these factors, there are various explanations for the observed paths: The path changes are caused either by a deflection of the shear band, by the blocking and subsequent renucleation of a new shear band, or by several nascent shear bands growing together. The unhindered "passing" of a precipitate can be explained either by a temporary path change of the shear band or by the participation of the precipitate in the plastic deformation. Because of the necessarily limited amount of data that can be obtained in the experiment, we undertake MD simulations to test the aforementioned hypotheses and investigate their relation to the sample geometry.

III. SIMULATION

A. Simulation setup and analysis

In order to gain more insights into the nanoscale mechanisms of shear-band interaction with precipitates, we perform a number of MD computer simulations, which allow for an "*in situ*" observation of shear-band propagation. We use the software LAMMPS [40] to quench metallic-glass samples, insert precipitates, and perform mechanical testing. The simulated metallic glass is a $Cu_{64}Zr_{36}$ alloy modeled with a Finnis–Sinclair-type potential by Mendelev *et al.* [41]. Metallic-glass samples with dimensions $10 \times 10 \times 10$ and $20 \times 20 \times 20$ nm^3 are prepared by melting the material at 2000 K and subsequent quenching to 50 K with a cooling rate of 0.01 K/ps.
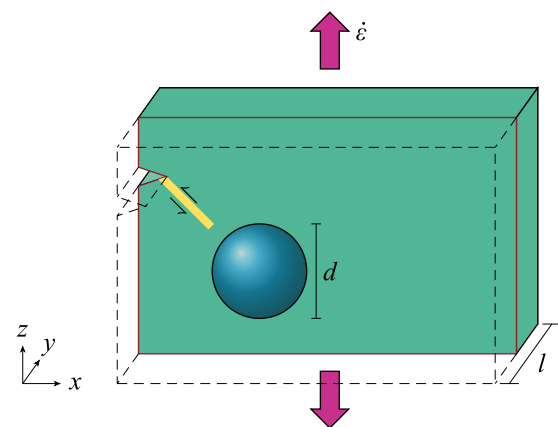

FIG. 4.   Schematic simulation setup. The picture shows a cut through the three-dimensional simulation box in the xz plane at $l/2$. A notch is inserted to control the origin of the shear band (yellow). The spherical precipitate is shown in blue. The box has open boundaries in the x direction and is otherwise periodic. A constant strain rate is applied in the z direction.

We use the sample geometry illustrated in Fig. 4 to investigate the influence of preexisting precipitates on an approaching shear band. Size effects are studied by varying the diameter d of the precipitates and by controlling the distance between periodic precipitate images by varying the box width l. Sample sizes are 120 nm $\times l \times$ 60 nm, with $l = 10$, 20, 30, and 40 nm. With a single precipitate per simulation box, this corresponds to number densities for the precipitates of $1.4 \times 10^{22}/m^3$, $6.9 \times 10^{21}/m^3$, $4.6 \times 10^{21}/m^3$, and $3.5 \times 10^{21}/m^3$, respectively. The Cu-Zr glass samples are replicated to reach the desired box dimensions, and spherical precipitates with diameters from 3 to 40 nm are inserted. For this, a hole is cut into the glass matrix with a size chosen to accommodate the precipitate without overlapping atoms. For the CuZr precipitate, we use the experimentally observed $B2$ structure [42–45]. The $B19'$ structure, which is found in the precipitates in the experimental part of this paper, is a distortion of the $B2$ structure [39]. A notch controls the origin of the shear band and makes sure that it always hits the precipitate. Periodic boundary conditions are applied in the y and z directions and open boundaries in the x direction. The resulting structure is equilibrated at 50 K for 2 ns with a barostat at ambient pressure in periodic directions. After equilibration, no long-ranging stress field around the precipitate is left; any mismatches are accommodated by the glass during the interface creation.

The resulting composite samples are deformed at 50 K under a constant tensile strain rate of $\dot{\varepsilon} = 4 \times 10^7/s$ in the z direction up to a total strain of at least 10%. The trajectories from equilibrated to fully deformed samples are analyzed to observe the shear-band propagation path. The shear band is identified by using the von Mises local shear invariant η_i [46] as implemented in the visualization tool OVITO [47]. Atoms with a local shear greater than around 0.2 are assigned to the shear band. To observe plastic deformation events in the crystalline phase, we perform atomic structure identification, which can identify crystal structures, stacking faults, and other defects [48].

B. Wrapping and blocking

The first observed interaction mechanism between a propagating shear band and a preexisting precipitate is shown in Fig. 5 and Video 1. Here, the shear band wraps around the precipitate like a carpet moving over a small obstacle. The particle does not deform and simply moves along with one half of the glass matrix. We call this mechanism the *wrapping mechanism*. This kind of athermal mechanism is virtually unknown in crystalline materials. The closest analog in a crystal—dislocation climb—is purely thermally activated. It is therefore instructive to compare the two material classes, as shown in Fig. 6.

In a crystalline material, a dislocation moves on defined slip planes. A change of slip plane is possible only for the screw components of the dislocation [49], is connected with a high energy barrier, and is usually observed only in stage-III work hardening [50]. Therefore, the Orowan mechanism applies: The dislocation is bent around the obstacle and finally forms dislocation rings [Fig. 6(a)] [51]. These rings may pile up, thereby hardening the material. In a metallic glass, as in any isotropic material, all slip directions are equivalent. Only an applied external stress differentiates the directions. Under tensile stress, the planes oriented in 45° angles towards the tensile axis experience the highest resolved stress. An obstacle can be avoided simply by temporarily and locally changing the slip path, thereby wrapping around the obstacle [Fig. 6(b)]. Depending on the precipitate distance, this wrapping mechanism is observed for precipitates with diameters smaller than 25–35 nm in our simulations.

An alternative mechanism appears for increasing diameters and decreasing distances between precipitates: The shear band is *blocked* by the precipitate. This causes the simultaneous nucleation of a second shear band perpendicular to the first one on the opposite side of the precipitate as shown in Fig. 7 and in Video 2. Again, there is no slip transfer to the crystalline phase. The paths of the shear bands in this simulation and in the HRTEM image of the experimental sample [Fig. 3(e)] are comparable. Both show what looks like a shear band that starts to wrap around the precipitate but does not propagate further. In the experiment, though, no fully formed shear band appears perpendicular to the original one. This may be a result of the more complex stress state or the fact that a new shear band can nucleate at another precipitate that is not visible in the images. Still, a region resembling a nascent shear band appears perpendicular to the original propagation direction, strengthening the agreement with the simulation results.

A systematic investigation of the parameters of precipitate distance and size reveal a clear correlation with the mechanism. For a more quantitative analysis, we define an empirical parameter Λ, which is given by the ratio of the cross-sectional area A of the precipitate divided by the distance of precipitate centers l as shown in Fig. 8(a). Similar to the derivation of the Orowan stress, the crystalline volume fraction $f = V_{precipitates}/V$ can be estimated from the average crystallite distance by the relation [51]

$$l = \frac{d/2}{\sqrt{f}} \Leftrightarrow f = \frac{d^2}{4l^2}. \qquad (1)$$

Using that, we can express Λ only in terms of volume fraction and precipitate geometry:

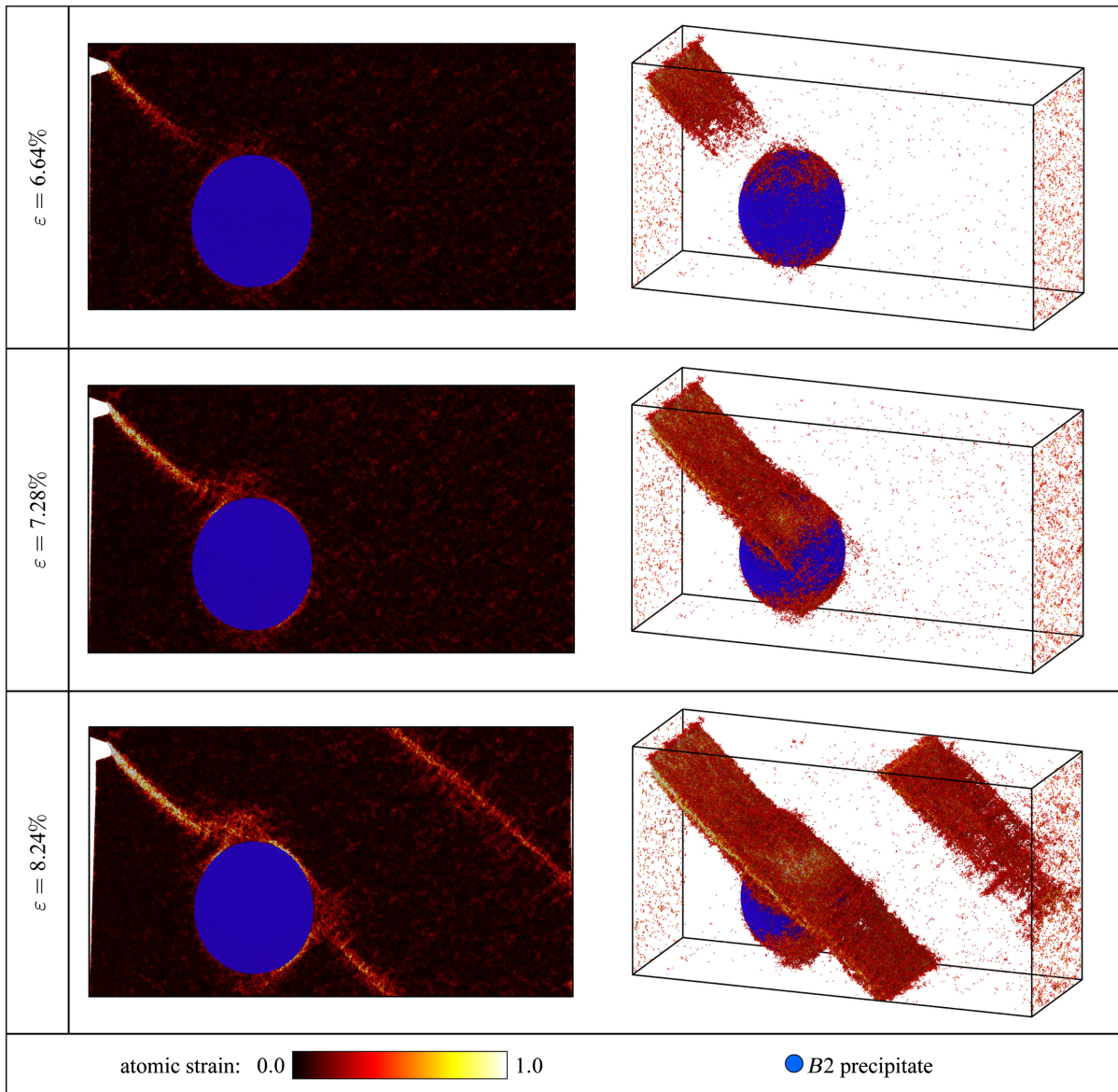$$\Lambda = \frac{A}{l} = \frac{A\sqrt{f}}{d/2}. \qquad (2)$$

FIG. 5.   Snapshots of a simulation with a 30-nm CuZr precipitate. The shear band wraps around the precipitate and continues unhindered. The glass matrix is colored according to the atomic strain. The precipitate atoms are shown in blue if they appear in the $B2$ structure; no defects are visible. The left column shows a cut through the middle of the precipitate. On the right, all atoms with $\eta_i < 0.3$ are deleted. A video version is provided in Video 1.

For nonoverlapping precipitates ($d < l$), it is $A = \pi d^2/4$, and Λ reduces to

$$\Lambda = \pi \frac{d}{2} \sqrt{f}. \qquad (3)$$

When the precipitates overlap ($d > l$), we reduce the area A to remove the overlapping circle segments. In the limit $l \to 0$, Λ corresponds to A/l of an infinite cylinder parallel to the shear-band front. Figure 8(b) shows a contour plot of the Λ parameter as a function of the precipitate diameter and distance. The data points in the plot represent results from our MD simulations, divided into those showing the wrapping and those showing the blocking mechanism. For the simulation geometry used in this work, there exists a given Λ that clearly separates the two mechanisms:

$$\Lambda_{\text{crit}} \approx 12.65 \text{ nm}. \qquad (4)$$

This Λ_{crit} is not universal, as, for example, the distance between precipitate and notch is not varied. A test simulation finds that increasing the distance from the notch and therefore increasing the shear-band length favors the wrapping mechanism.
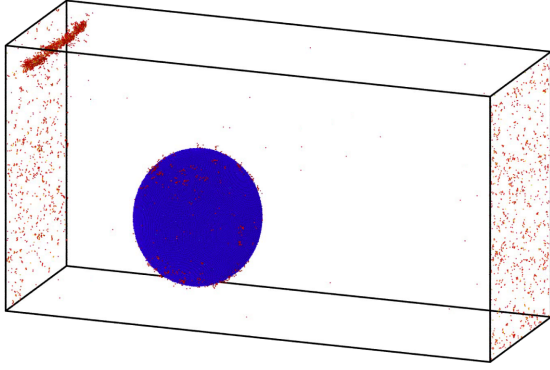
VIDEO 1.   Simulation of a shear band wrapping around a 30-nm CuZr precipitate as shown in Fig. 5.

Using these formulas, we can also estimate Λ for the experimental results. Given a number density of precipitates $n = 10^{20}$ m^{-3} and particle diameters of around 70 nm, we obtain

$$f = \frac{V_{\text{precipitates}}}{V} = n\frac{4}{3}\pi(35 \text{ nm})^3 \approx 1.8\%, \qquad (5)$$

$$\Lambda_{\text{exp}} = \pi \times 35 \text{ nm} \times \sqrt{1.8\%} \approx 14.7 \text{ nm} > \Lambda_{\text{crit}}. \quad (6)$$

This is consistent with the fact that the shear bands that are observed in the glass samples are blocked by the precipitates. Still, the value is close to Λ_{crit}, which means that slightly smaller precipitates (or precipitates that are not hit centrally, virtually decreasing the prefactor d) may be susceptible to wrapping.

Figure 9 shows examples of the stress-strain curves of samples that exhibit either the wrapping or the blocking mechanism. Neither a pronounced ductility nor significant strain hardening can be observed. This lack of strain hardening is in accordance with experimental data for tensile tests on Cu-Zr-based metallic glasses with crystalline precipitates [12–14]. It also fits with a recent study of compression tests of Cu-Zr-based metallic glass that finds
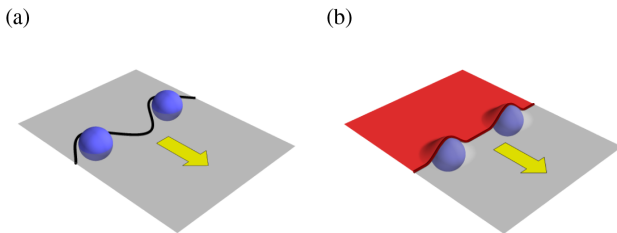

FIG. 6.   Comparison of the Orowan mechanism (a) with a shear band wrapping around precipitates (b). The slip plane is shown in gray, the precipitates in blue, the dislocation as a black line, and the shear band as a red plane. The precipitates can stop a dislocation because it must remain in a defined slip plane, while the shear band can temporarily leave its slip plane and continue unhindered afterwards.

an effect of particle size on mechanical parameters but no particle hardening [52].

C. Plastic deformation of the crystalline phase

The precipitates discussed until now were all "hard," i.e., not susceptible to plastic deformation under the simulation conditions: Because of the high antiphase-boundary energy in the $B2$ structure, superdislocations or twinning with respect to a martensitic transformation would be needed for a plastic deformation of the precipitates. The stress available at the shear-band tip is not sufficient to nucleate these defects, which explains why no plastic deformation of the crystalline phase can be observed in our simulations. In experiments, deformation-grown precipitates show twinning defects which may cause softening effects and make the precipitate susceptible to plastic deformation [21]. As a model for a softer precipitate, we thus exchange the $B2$ crystal phase for fcc copper.

For precipitates that are small relative to the shear-band width, the nanocrystals undergo mechanical dissolution [27,33]. This is also observed in our setup with 3-nm particles as shown in Fig. 10. In samples with larger diameters, the precipitates do not deform plastically but instead show the same wrapping and blocking interactions as described before for the "hard" precipitates. Even if the (111) glide plane is oriented parallel to the shear-band direction to maximize resolved shear stress on the preferred fcc slip plane, we do not observe slip transfer into the nanoprecipitate. The corresponding stress-strain curves are shown in Fig. 11(a). To explain this, we estimate the critical stress for heterogeneous dislocation nucleation in fcc copper by shearing a nanowire on the (111) plane in the [110] direction [see Fig. 11(c) for the simulation setup]. For this, we hold the lower layer of atoms fixed and move the top layer of atoms with a constant velocity in the [110] direction to achieve volume-conserving shear. The diameter of the nanowire is 10 nm, i.e., on the order of the smaller precipitates to maximize surface effects. The resulting shear stress over shear curve is also plotted in Fig. 11(a). The yield stress of the nanowire, τ_{crit}, is an estimate for the stress needed for heterogeneous dislocation nucleation at the glass-precipitate interface. For comparing the shear stress in the nanowire with the tensile stress in the composite, we assume a Schmid factor of 0.5 and scale the tensile axis by a factor of 0.5 compared to the shear stress axis. This graphically estimates an upper bound of the shear stress τ_m that arrives at the precipitate; corresponding values are given in Table I. The upper bound of the estimated maximum resolved shear stress in the composite is comparable to the lower bound for heterogeneous dislocation nucleation. While this suggests that dislocation nucleation may be possible, it is important to keep in mind that the
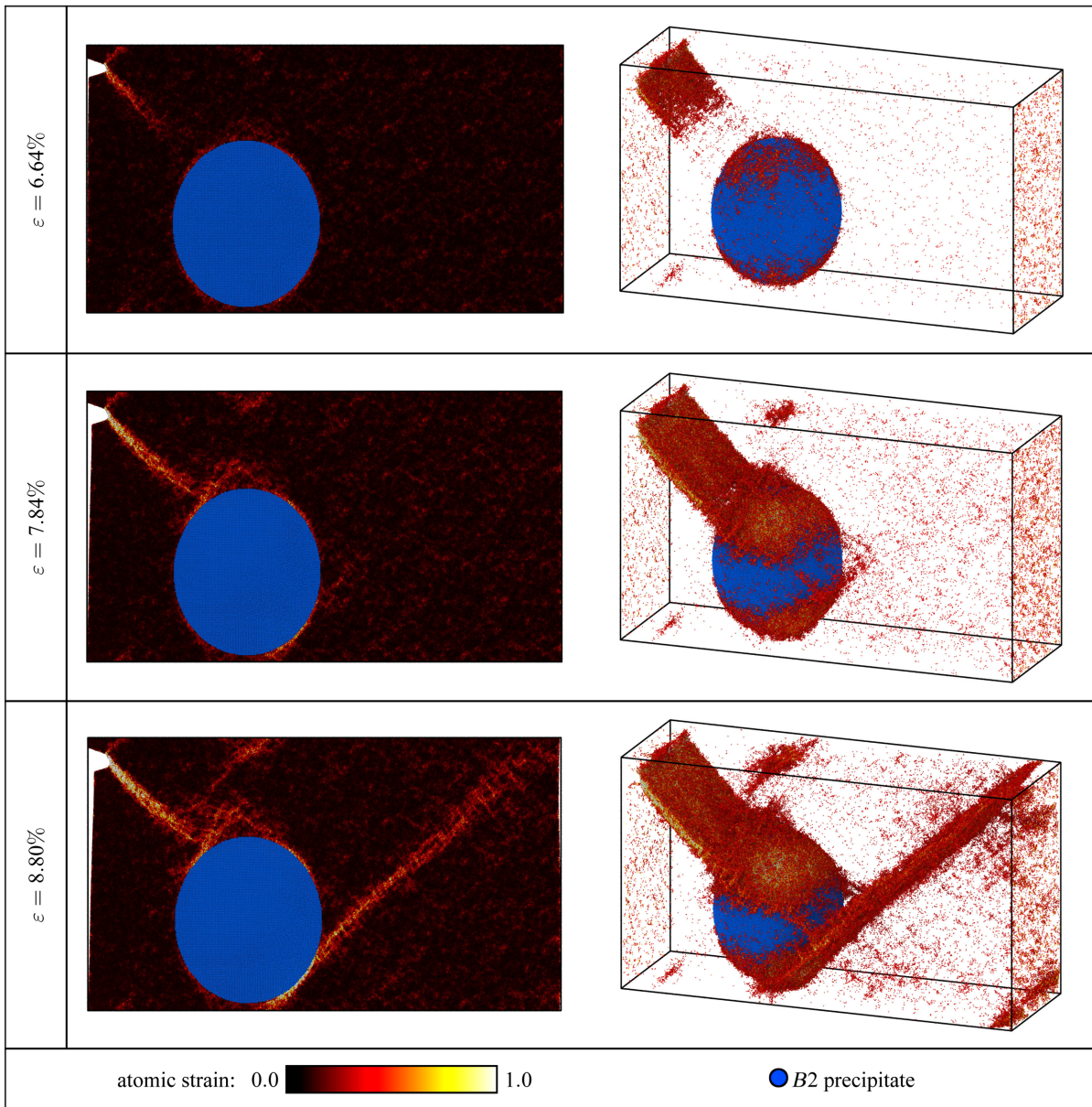
FIG. 7.   Snapshots of a simulation with a 37.5-nm CuZr precipitate. The shear band is blocked by the precipitate, while a second shear band is immediately nucleated in another plane of high resolved shear stress. The glass matrix is colored according to the atomic strain. The precipitate atoms are shown in blue if they appear in the $B2$ structure; no defects are visible. The left column shows a cut through the middle of the precipitate. On the right, all atoms with $\eta_i < 0.3$ are deleted. A video version is provided in Video 2.

nanowire shear test provides only a lower bound in an idealized case and that the actual shear stress available to nucleate a dislocation may be lower than $0.5\sigma_z$, which is why no plastic deformation of the precipitate is observed. Evidently, the value of τ_{crit} in the Mendelev potential is much too high, and therefore the Cu precipitates are "harder" than expected, which is a deficiency of the potential model for pure Cu.

Because of this, we switch to a different potential, which provides a better description of crystalline Cu.

The Finnis–Sinclair-type potential by Ward *et al.* [53] is created by using preexisting potentials for the elemental phases [54] and fitting the cross terms to the intermetallic phases. As shown in the Appendix, this potential has a more realistic unstable stacking-fault energy and critical stress for homogeneous dislocation nucleation than the Mendelev potential. As shown in Fig. 11(b) and Table I, the critical stress for heterogeneous nucleation is much lower than even the steady-state stress in the composite, easily allowing plastic deformation of the particle.
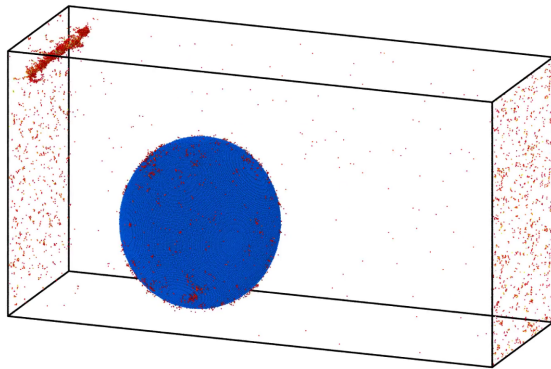
VIDEO 2.   Simulation of a shear band being blocked by a 37.5-nm CuZr precipitate as shown in Fig. 7.

The results for a 30-nm copper precipitate are shown in Fig. 12 and in Video 3. The precipitate is *cut* by the shear band, and slip transfer through the particle can be observed. This mechanism replaces the previously
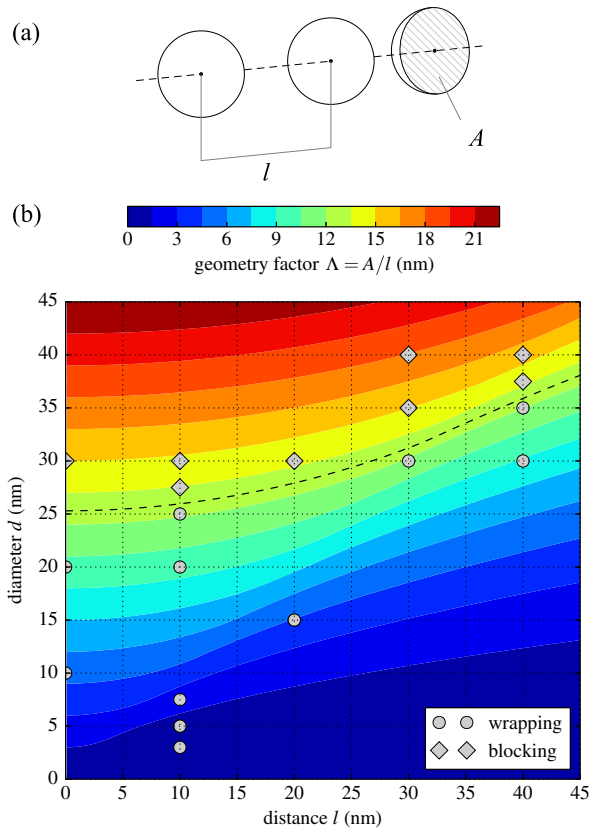

FIG. 8.   Influence of the precipitate size and distance on the mechanism. (a) Explanation of the parameter l, distance of the precipitates, and A, the area of a cut through the precipitate. (b) shows a contour plot of the empirical geometry factor $\Lambda = A/l$. The dashed line shows the critical value of Λ for a transition from the wrapping to the blocking mechanism. Data points are MD simulations. The data points at $l = 0$ nm are infinite cylinders along the y axis, representing the case of overlapping spheres with infinitesimally small distances between their centers.
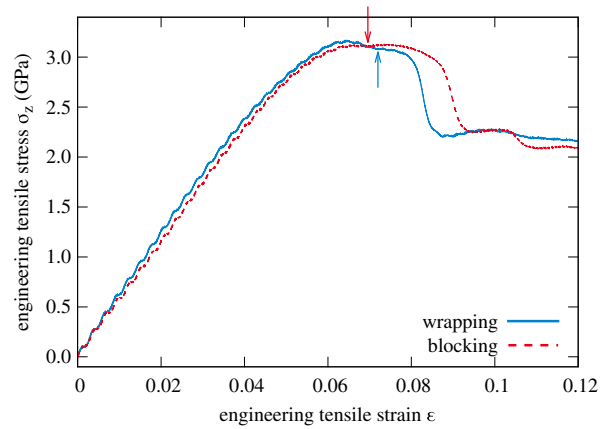

FIG. 9.   Stress-strain curves of samples which exhibit the wrapping or blocking mechanisms. The arrows indicate when the shear band hits the precipitate.

discussed blocking of the shear band if the nanoprecipitates are "soft": For the crystal to partake in the plastic deformation, dislocation nucleation must be possible at shear stresses below the highest resolved shear stress in the metallic glass at yield. Despite the participation of the crystalline phase in the plastic deformation, the stress-strain curve in Fig. 11(b) shows the distinctive stress drop connected with a single critical shear band and no strain hardening. The reason is that in this setup the crystalline phase accounts only for roughly 5 vol % of the sample. This means that the macroscopic mechanical properties are still dominated by the metallic glass. As the shear band can simply cut through the crystal, the precipitate poses no obstacle to the percolation of the critical shear band. For a larger crystalline volume, a ductile crystalline phase could possibly also constrain the shear bands [11].
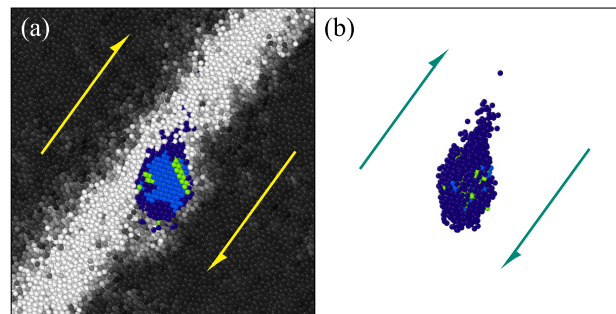

FIG. 10.   Mechanical dissolution of a 3-nm copper particle in a shear band. The gray-scale color coding shows atomic strain η_i from 0.0 (black) to 1.0 (white). The precipitate is shown in color: Light blue atoms are in the fcc structure, green atoms are in a stacking fault, and dark blue atoms are disordered. The arrows indicate the shear direction. (a) shows a cut through the middle of the nanoprecipitate, while (b) shows only the atoms that initially belonged to the nanoprecipitate.
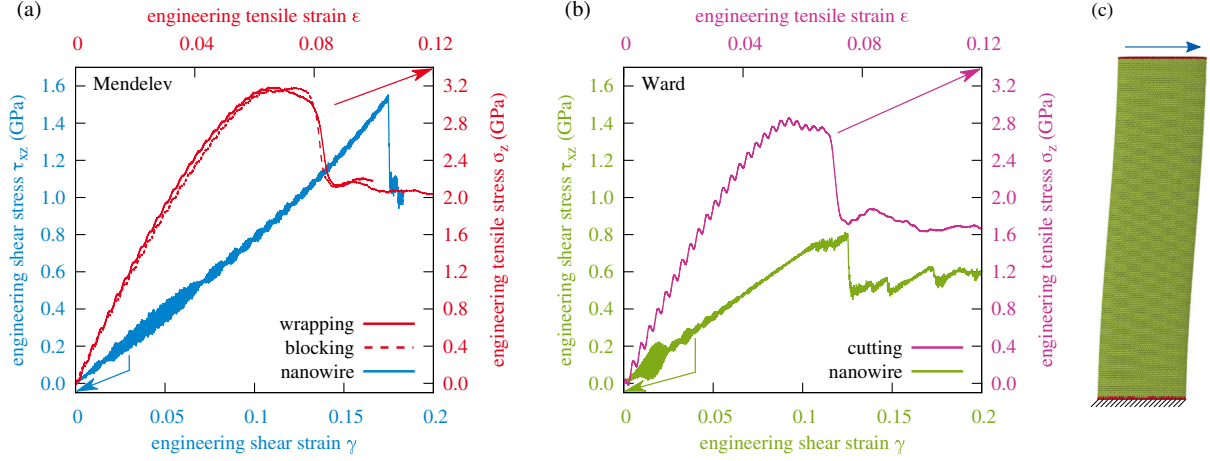
FIG. 11.   Stress-strain curves for the composites with fcc copper precipitates and for a 10-nm copper nanowire. (a) Curves from simulations with the Mendelev potential. The copper precipitates do not deform plastically and show similar behavior to the CuZr precipitates discussed earlier. The curve of the copper nanowire explains this: The yield stress, and therefore the critical shear stress, is higher than the highest resolved shear stress in the steady state in the composite. To be able to compare the tensile stress in the composite with the shear stress in the nanowire, the tensile stress axis is scaled with a factor of 0.5 corresponding to the Schmid factor for the plane of highest resolved shear stress. (b) Curves from simulations with the Ward potential. Now the critical stress for heterogeneous dislocation nucleation is lower than the steady-state stress in the composite, and the precipitate deforms plastically. (c) The simulation setup for the nanowire. The wire is sheared in the [110] direction of the fcc crystal structure on the (111) plane. The red atoms are fixed, and the atoms on the top are shifted with a constant velocity to shear the nanowire.

IV. DISCUSSION

Using TEM imaging, we observe shear-band bending around or close to precipitates, an attraction of shear bands to the precipitates, and shear bands being blocked by precipitates. In our MD simulations, we find four mechanisms of interaction between shear bands and precipitates:

  (i) precipitates that are small relative to the shear-band width dissolve mechanically,
  (ii) shear bands can wrap around precipitates,
  (iii) shear bands are blocked by precipitates, and
  (iv) shear bands cut through precipitates, and slip transfer into the crystalline phase takes place.

Which of these mechanisms is active for a given precipitate depends on the competition between the propagation of the existing shear band, the heterogeneous nucleation of a new shear band, and the heterogeneous dislocation nucleation in the precipitate. The wrapping-to-blocking transition can be quantified by the parameter $\Lambda = A/l \propto A\sqrt{f}/d$. Below $\Lambda = \Lambda_{\text{crit}}$, the wrapping mechanism is favored. This value can be explained by the following simple argument. When

TABLE I.   Comparison of maximum stress σ_m and the corresponding resolved shear stress τ_m with the critical shear stress τ_{crit} for heterogeneous dislocation nucleation in copper in the Mendelev and Ward potentials. The calculation of the resolved shear stress assumes a Schmid factor of 0.5.

	σ_m (GPa)	τ_m (GPa)	τ_{crit} (GPa)
Mendelev	3.2	1.6	1.55
Ward	2.9	1.45	0.75

the shear band reaches a precipitate which does not deform, the shearing of the sample momentarily stops. The stress τ_{SB} in the shear band resulting from the externally applied tensile stress σ_{ext} amounts to

$$\tau_{\text{SB}} = \frac{1}{2}\sigma_{\text{ext}}. \qquad (7)$$

This stress acts mainly on the shear-band front, allowing us to write

$$F_{\text{ext}} \approx \tau_{\text{SB}} \times l \times h_{\text{SB}} = \frac{\sigma_{\text{ext}}}{2} l h_{\text{SB}}, \qquad (8)$$

where h_{SB} is the width of the shear band. At the moment that the shear band hits the precipitate, the force F_{ext} must be equal to a reaction force F_{back} from the precipitate (*actio est reactio*). Using the projected precipitate area A (cf. Fig. 13), we can convert that force into a normal stress:

$$\sigma_A^n = \frac{F_{\text{back}}}{A/2}. \qquad (9)$$

We assume that F_{ext} predominantly acts on one half of the obstacle (area $A/2$), which is supported by the deformation pattern of the plastically deformed particle (Fig. 12 and Video 3). This back stress results in a shear stress $\tau_{\text{wrap}} \approx 0.5\sigma_A^n$ in the plane of the wrapping shear band (green shear band in Fig. 13). With $F_{\text{back}} = F_{\text{ext}}$, it is

$$\sigma_A^n = \frac{F_{\text{ext}}}{A/2} = \frac{\sigma_{\text{ext}} l h_{\text{SB}}}{A} = 2\tau_{\text{wrap}}. \qquad (10)$$
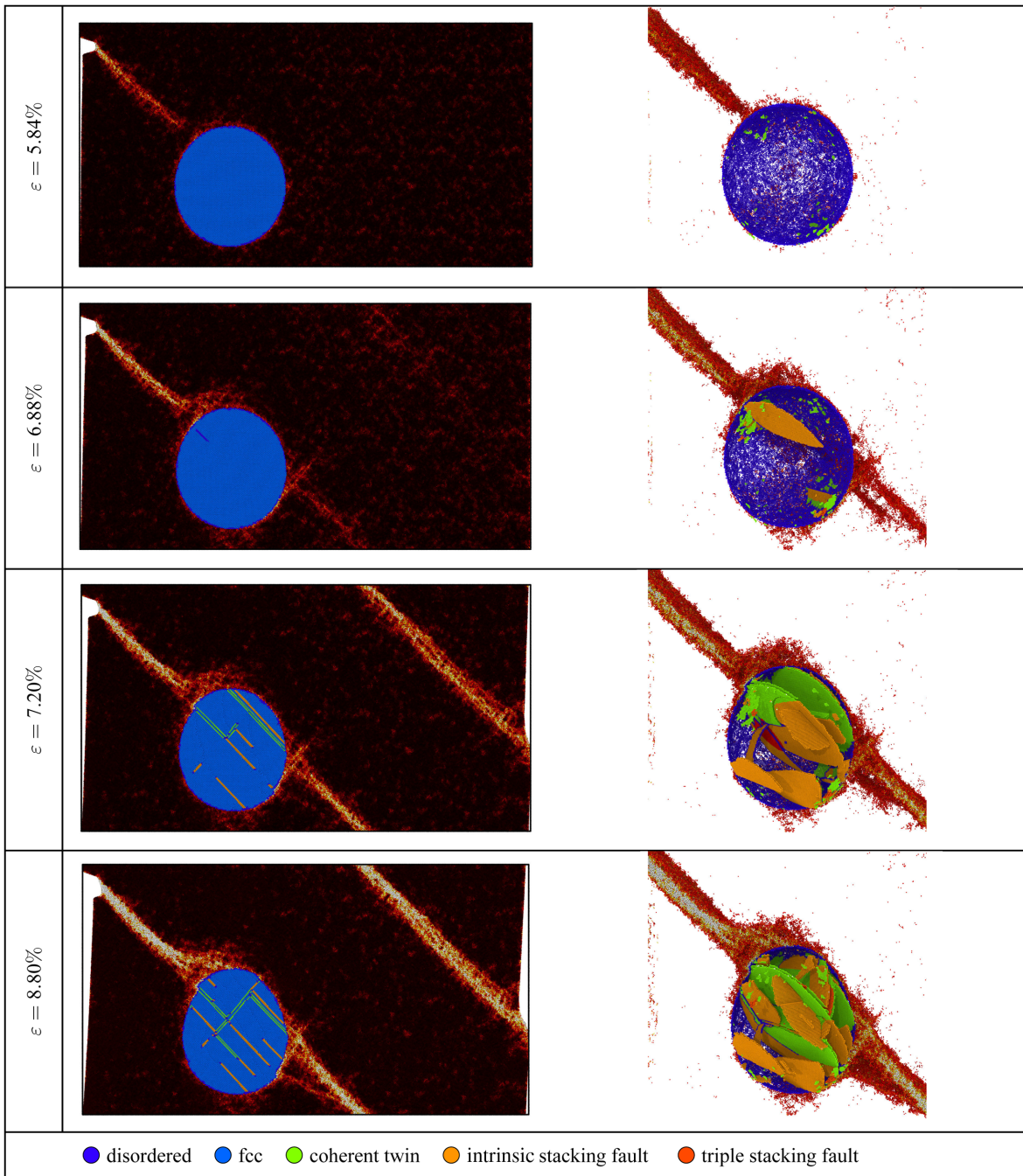
FIG. 12.   Snapshots of a simulation with a 30-nm copper precipitate. This simulation uses the Ward potential, in which the critical stress for dislocation nucleation is realistic. As the precipitate is sufficiently soft, the shear band can cut through it. The glass matrix is colored according to the atomic strain (the same scale as Figs. 5 and 7). Defects in the fcc crystal structure are colored according to the legend. The left column shows a cut through the middle of the precipitate. On the right, all atoms with $\eta_i < 0.3$ and all fcc-coordinated atoms are deleted. A video version is provided in Video 3.

τ_{wrap} must surpass a critical value $\tilde{\tau}_{\mathrm{wrap}}$ to allow the initiation of the wrapping mechanism; otherwise, the shear band simply stops propagating. This is not observed in our simulations, suggesting that σ_{ext} at yield is greater than

$$\tilde{\sigma}_{\mathrm{ext}} = \frac{2A\tilde{\tau}_{\mathrm{wrap}}}{lh_{\mathrm{SB}}}. \qquad (11)$$

The competing mechanism, blocking the shear band and nucleating a new one (red shear band in Fig. 13), can simply be expressed by a critical shear stress $\tilde{\tau}_{\mathrm{nucl}}$. Because of the low temperature in the simulation and a stress close to the yield stress, we consider only the athermal case and do not invoke a nucleation term which takes into account the relative volume of the interface.
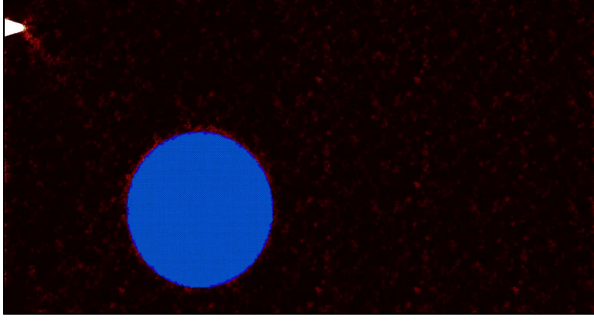
VIDEO 3.   Simulation of a shear band cutting a 30-nm copper precipitate as shown in Fig. 12.

With $\tau_{\mathrm{nucl}} = 0.5\sigma_{\mathrm{ext}}$, the transition from wrapping to blocking takes place where

$$2\tilde{\tau}_{\mathrm{nucl}} = \tilde{\sigma}_{\mathrm{ext}} = \frac{2A\tilde{\tau}_{\mathrm{wrap}}}{l h_{\mathrm{SB}}}, \qquad \text{giving} \qquad (12)$$

$$\frac{A}{l} = \Lambda_{\mathrm{crit}} = \frac{\tilde{\tau}_{\mathrm{nucl}}}{\tilde{\tau}_{\mathrm{wrap}}} h_{\mathrm{SB}}. \qquad (13)$$

This derivation also works in the case of externally applied shear stress, by replacing σ_{ext} with $2\tau_{\mathrm{ext}}$.

Assuming that nucleating a new shear band at the interface and propagating the wrapping shear band along the interface have similar critical stresses, we can simplify Eq. (13) to

$$\Lambda_{\mathrm{crit}} \approx h_{\mathrm{SB}}. \qquad (14)$$

Shear bands in Cu-Zr-based glasses have widths of around 10 nm [55], which fits to the $\Lambda_{\mathrm{crit}} = 12.65$ nm observed in our model systems. As stated earlier, the wrapping mechanism becomes more favorable again if the shear band is longer before it hits the precipitate. The reason is that
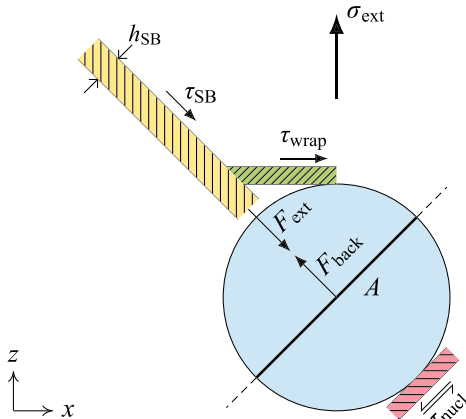

FIG. 13.   Projection of the forces and stresses acting around the precipitate (blue circle) onto the xz plane. Shear bands are shown as hatched areas, where yellow signifies the arriving shear band, green the path for wrapping, and red the site for the nucleation of a new shear band.

this gives the shear band time to deviate slightly from its path, so that it does not hit the precipitate centrally, thus effectively reducing A. In practice, this is not a big problem, as the free shear-band length is constrained to approximately l anyway due to the distribution of precipitates in the sample. While this derivation is only approximate, it seems to be sufficient to explain the observed phenomena and guide future efforts in tuning the mechanical behavior of crystal-glass composites. Furthermore, it is easily possible to explain the fourth mechanism, a slip transfer into the crystalline phase. The critical stress for heterogeneous nucleation of a dislocation in the precipitate $\tilde{\tau}_{\mathrm{disl}}$ must be provided by the shear band via $\tau_{\mathrm{SB}} = 0.5\sigma_{\mathrm{ext}}$. If $\tilde{\tau}_{\mathrm{disl}} < \tilde{\tau}_{\mathrm{nucl}}$, we can simply replace $\tilde{\tau}_{\mathrm{nucl}}$ by $\tilde{\tau}_{\mathrm{disl}}$ in Eqs. (12) and (13), thereby replacing the blocking mechanism with the plastic deformation of the precipitate. A lowered $\tilde{\tau}_{\mathrm{disl}}$ also lowers Λ_{crit}.

A simple deflection of the shear band is not observed and seems unlikely, as any deviation of the shear band from its path leads to a reduced resolved shear stress and thereby to a driving force to put it back "on track." Contrary to the experiment, a change of shear-band path towards the precipitate is also not observed. Because the precipitates in our simulations are inserted artificially and do not have a large stress field around them, this seems reasonable. In thermally grown precipitates, a stress field due to density mismatch between glass and crystal seems likely. Still, due to the geometry of the MD simulations, the shear band has two equivalent propagation pathways from the notch but always chooses the one leading towards the precipitate. This seems to be a weaker form of the attraction observed experimentally.

With these results, we can attempt an explanation of the experimentally observed phenomena. First of all, the blocking of the shear band is a one-to-one correspondence between simulation and experiment. Comparing Fig. 3(e) with Fig. 7, we can see that the path of the shear band looks identical. The shear band wraps partly around the precipitate but is then blocked and does not propagate. Contrary to the simulation, no fully formed shear band but only a small shear-band-like region appears at the opposite crystal-glass interface. This may be a result of either the more complex stress state in the experiment or the fact that other precipitates are available at which the new shear band may nucleate. For the winding shear-band path, we can now exclude a simple deflection as discussed above. A possible explanation would be the concurrent nucleation of nascent shear bands at the crystal-glass interfaces which grow together into a single mature shear band. While the interfaces are known to be nucleation sources for shear bands [27–29], our simulations show that the nucleation of a shear band at a stress concentrator like a notch or a crack always takes precedence to nucleation at interfaces or surfaces. The shear bands shown in the TEM images all originate from crack tips, making it unlikely that the shear band shown in Fig. 2 consists of several concurrently nucleated shear bands. This
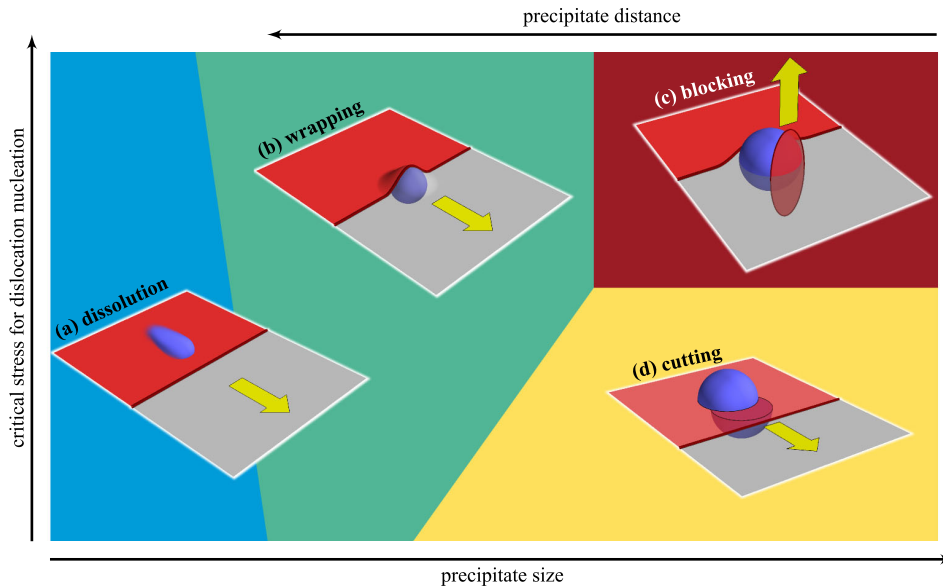
FIG. 14. Schematic view of different mechanisms for the interaction of a shear band with a crystalline precipitate. With increasing precipitate sizes, the dissolution of the precipitate is first replaced by the wrapping mechanism. Depending on the critical stress for dislocation nucleation, wrapping is replaced by blocking or cutting. Wrapping can be favored by increasing the precipitate distance.

leaves the explanation that this winding path is a series of subsequent blocking and renucleation events.

The observed Λ_{crit} corresponds to precipitate diameters somewhere between 20 and 40 nm, depending on the interparticle distance. This critical diameter is on the order of magnitude reported in several experimental studies for twinning in $B2$ crystals in Cu-Zr-Al-based metallic glasses of 20 ± 5 nm [14,56]. It also fits an experimental work on Al-based glasses, where crystallites growing during deformation are sheared apart when they reach a critical size of about 10 nm [57]. $Cu_{50}Zr_{45}Ti_5$ metallic glasses exhibit a critical size of about 9 nm for twinning of $B2$ precipitates [52]. The interparticle distances in these experiments are on the same order of magnitude as for our simulations. This supports an explanation of a transition from wrapping to slip transfer in these systems.

Figure 14 summarizes the competition between the different mechanisms. Mechanical dissolution of the crystalline particles occurs only if their size is comparable to the shear-band size [33]. With further increasing precipitate sizes, the shear band can still wrap around the obstacle until the size reaches a threshold value. This critical size also depends on the precipitate distance, as discussed before, expressed in the parameter $\Lambda_{crit}(d, l)$. If wrapping is no longer possible, a precipitate which reacts only elastically to the applied stress will block the shear band. If the precipitate is susceptible to plastic deformation, slip transfer into the precipitate will take place.

Concerning the mechanical performance of such *in situ* composites with crystalline precipitates that originate from nucleation and growth within the glass, the current results suggest that the discussed geometrical effects serve to improve the macroscopic mechanical performance. None of the presented mechanisms seem to inhibit the percolation of a critical shear band, yet catastrophic slip along a shear band leading to complete failure is delayed in the case of winding shear bands due to the increase of the shear-band path length as well as the raised activation barriers for slip along shear bands that have a more complex topology. The wrapping mechanism does not pose an obstacle to shear-band propagation but can be avoided by appropriate adjustment of the crystalline volume fraction and precipitate diameter. "Soft" precipitates additionally open possibilities to adjust the plastic deformation by participating in it. Consistently, by increasing the volume fraction of the ductile crystalline phase, the constraints on shear-band propagation can be increased, immediate failure can be prevented (cf. Ref. [11]), and the composite displays macroscopic mechanical behavior according to a mixing rule, further allowing one to tailor the properties.

V. CONCLUSIONS

Using TEM imaging, we observe shear-band bending around or close to precipitates, an attraction of shear bands to the precipitates, and shear bands being blocked by precipitates. MD simulations reveal that the shear-band bending is most likely the result of the subsequent blocking and renucleation of shear bands. Moreover, we identify shear bands wrapping around precipitates and slip transfer into the crystalline phase. By describing the competition between the critical stress for wrapping, the nucleation of a new shear band, and the nucleation of dislocations in the crystal, we could derive a mechanism map for metallic glasses with nanocrystalline precipitates. This detailed description of shear-band propagation not only helps to understand the mechanical failure of these composites but also aids in tuning them.

ACKNOWLEDGMENTS

APPENDIX: GENERALIZED STACKING-FAULT ENERGY IN FCC COPPER

The generalized stacking-fault energy in fcc copper is calculated by using both Mendelev [41] and Ward [53,54]
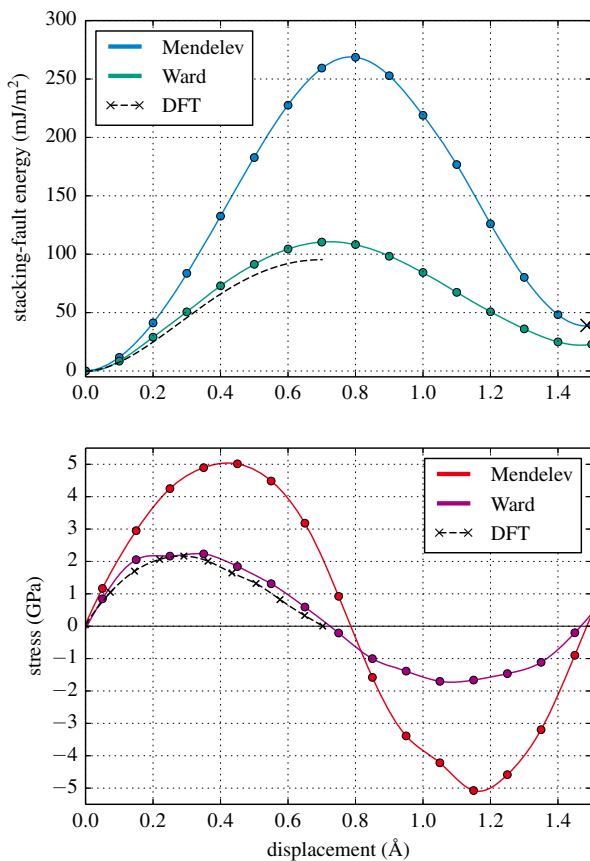

FIG. 15. Generalized stacking-fault energies (top) and the resulting shear stresses (bottom) for fcc copper. The DFT values for the stress curve are from Ogata, Li, and Yip [58], and the corresponding stacking-fault energies are approximated by using a numerical integration of the stress data.

potentials. Density-functional theory (DFT) calculations from Ogata, Li, and Yip [58] using the same method are used for comparison. This is plotted in Fig. 15. The Ward potential much more accurately describes the stacking-fault energy than the Mendelev potential, which has a critical stress for homogeneous dislocation nucleation which is more than 2 times too high.

[1] A. Inoue, Stabilization of metallic supercooled liquid and bulk amorphous alloys, Acta Mater. **48**, 279 (2000).

[2] M. F. Ashby and A. L. Greer, Metallic glasses as structural materials, Scr. Mater. **54**, 321 (2006).

[3] C. Fan and A. Inoue, Improvement of mechanical properties by precipitation of nanoscale compound particles in Zr-Cu-Pd-Al amorphous alloys, Mater. Trans., JIM **38**, 1040 (1997).

[4] S.-W. Lee, M.-Y. Huh, E. Fleury, and J.-C. Lee, Crystallization-induced plasticity of Cu-Zr containing bulk amorphous alloys, Acta Mater. **54**, 349 (2006).

[5] K. Hajlaoui, A. R. Yavari, A. LeMoulec, W. J. Botta, F. G. Vaughan, J. Das, A. L. Greer, and Å. Kvick, Plasticity induced by nanoparticle dispersions in bulk metallic glasses, J. Non-Cryst. Solids **353**, 327 (2007).

[6] J. Fornell, E. Rossinyol, S. Suriñach, M. D. Baró, W. H. Li, and J. Sort, Enhanced mechanical properties in a Zr-based metallic glass caused by deformation-induced nanocrystallization, Scr. Mater. **62**, 13 (2010).

[7] J. B. Li, J. S. C. Jang, S. R. Jian, K. W. Chen, J. F. Lin, and J. C. Huang, Plasticity improvement of ZrCu-based bulk metallic glass by ex situ dispersed Ta particles, Mater. Sci. Eng. A **528**, 8244 (2011).

[8] M. Calin, J. Eckert, and L. Schultz, Improved mechanical behavior of Cu-Ti-based bulk metallic glass by *in situ* formation of nanoscale precipitates, Scr. Mater. **48**, 653 (2003).

[9] C. C. Hays, C. P. Kim, and W. L. Johnson, Microstructure Controlled Shear Band Pattern Formation and Enhanced Plasticity of Bulk Metallic Glasses Containing *In Situ* Formed Ductile Phase Dendrite Dispersions, Phys. Rev. Lett. **84**, 2901 (2000).

[10] C. C. Hays, C. P. Kim, and W. L. Johnson, Improved mechanical behavior of bulk metallic glasses containing *in situ* formed ductile phase dendrite dispersions, Mater. Sci. Eng. A **304–306**, 650 (2001).

[11] D. C. Hofmann, J.-Y. Suh, A. Wiest, G. Duan, M.-L. Lind, M. D. Demetriou, and W. L. Johnson, Designing metallic glass matrix composites with high toughness and tensile ductility, Nature (London) **451**, 1085 (2008).

[12] S. Pauly, S. Gorantla, G. Wang, U. Kühn, and J. Eckert, Transformation-mediated ductility in CuZr-based bulk metallic glasses, Nat. Mater. **9**, 473 (2010).

[13] N. S. Barekar, S. Pauly, R. B. Kumar, U. Kühn, B. K. Dhindaw, and J. Eckert, Structure-property relations in bulk metallic Cu-Zr-Al alloys, Mater. Sci. Eng. A **527**, 5867 (2010).

[14] S. Pauly, G. Liu, S. Gorantla, G. Wang, U. Kühn, D. H. Kim, and J. Eckert, Criteria for tensile plasticity in Cu-Zr-Al bulk metallic glasses, Acta Mater. **58**, 4883 (2010).

[15] J. W. Qiao, T. Zhang, F. Q. Yang, P. K. Liaw, S. Pauly, and B. S. Xu, A tensile deformation model for *in-situ* dendrite/metallic glass matrix composites, Sci. Rep. **3**, 2816 (2013).

[16] C. Paul Kim, Y. S. Oh, S. Lee, and N. J. Kim, Realization of high tensile ductility in a bulk metallic glass composite by the utilization of deformation-induced martensitic transformation, Scr. Mater. **65**, 304 (2011).

[17] Z. Liu, R. Li, G. Liu, K. Song, S. Pauly, T. Zhang, and J. Eckert, Pronounced ductility in CuZrAl ternary bulk metallic glass composites with optimized microstructure through melt adjustment, AIP Adv. **2**, 032176 (2012).

[18] F.-F. Wu, K. C. Chan, S.-T. Li, and G. Wang, Stabilized shear banding of ZrCu-based metallic glass composites under tensile loading, J. Mater. Sci. **49**, 2164 (2014).

[19] X. L. Fu, Y. Li, and C. A. Schuh, Mechanical properties of metallic glass matrix composites: Effects of reinforcement character and connectivity, Scr. Mater. **56**, 617 (2007).

[20] K. K. Song, S. Pauly, B. A. Sun, J. Tan, M. Stoica, U. Kühn, and J. Eckert, Correlation between the microstructures and the deformation mechanisms of CuZr-based bulk metallic glass composites, AIP Adv. **3**, 012116 (2013).

[21] Q. P. Cao, J. F. Li, Y. Hu, A. Horsewell, J. Z. Jiang, and Y. H. Zhou, Deformation-strengthening during rolling $Cu_{60}Zr_{20}Ti_{20}$ bulk metallic glass, Mater. Sci. Eng. A **457**, 94 (2007).

[22] M. Chen, A. Inoue, W. Zhang, and T. Sakurai, Extraordinary Plasticity of Ductile Bulk Metallic Glasses, Phys. Rev. Lett. **96**, 245502 (2006).

[23] G. Wilde and H. Rösner, Nanocrystallization in a shear band: An *in situ* investigation, Appl. Phys. Lett. **98**, 251904 (2011).

[24] J. Bokeloh, S. V. Divinski, G. Reglitz, and G. Wilde, Tracer Measurements of Atomic Diffusion inside Shear Bands of a Bulk Metallic Glass, Phys. Rev. Lett. **107**, 235503 (2011).

[25] Y. Wu, D. Q. Zhou, W. L. Song, H. Wang, Z. Y. Zhang, D. Ma, X. L. Wang, and Z. P. Lu, Ductilizing Bulk Metallic Glass Composite by Tailoring Stacking Fault Energy, Phys. Rev. Lett. **109**, 245506 (2012).

[26] J. Corteen, M. Rainforth, and I. Todd, A mathematical approach to transformation toughening in bulk metallic glasses, Scr. Mater. **65**, 524 (2011).

[27] K. Albe, Y. Ritter, and D. Şopu, Enhancing the plasticity of metallic glasses: Shear band formation, nanocomposites and nanoglasses investigated by molecular dynamics simulations, Mech. Mater. **67**, 94 (2013).

[28] A. Zaheri, F. Abdeljawad, and M. Haataja, Simulation study of mechanical properties of bulk metallic glass systems: Martensitic inclusions and twinned precipitates, Model. Simul. Mater. Sci. Eng. **22**, 085008 (2014).

[29] Y. S. Wang, G. J. Hao, Y. Zhang, J. P. Lin, L. Song, and J. W. Qiao, The role of the interface in a Ti-based metallic glass matrix composite with *in situ* dendrite reinforcement, Surf. Interface Anal. **46**, 293 (2014).

[30] Y. Wang, J. Li, A. V. Hamza, and T. W. Barbee, Ductile crystalline-amorphous nanolaminates, Proc. Natl. Acad. Sci. U.S.A. **104**, 11155 (2007).

[31] B. Arman, C. Brandl, S. N. Luo, T. C. Germann, A. Misra, and T. Çağin, Plasticity in $Cu(111)/Cu_{46}Zr_{54}$ glass nanolaminates under uniaxial compression, J. Appl. Phys. **110**, 043539 (2011).

[32] C. Brandl, T. C. Germann, and A. Misra, Structure and shear deformation of metallic crystalline-amorphous interfaces, Acta Mater. **61**, 3600 (2013).

[33] A. C. Lund and C. A. Schuh, Critical length scales for the deformation of amorphous metals containing nanocrystals, Philos. Mag. Lett. **87**, 603 (2007).

[34] Y. Shi and M. L. Falk, A computational analysis of the deformation mechanisms of a nanocrystal-metallic glass composite, Acta Mater. **56**, 995 (2008).

[35] H. Rösner, M. Peterlechner, C. Kübel, V. Schmidt, and G. Wilde, Density changes in shear bands of a metallic glass determined by correlative analytical transmission electron microscopy, Ultramicroscopy **142**, 1 (2014).

[36] G. Kumar, T. Ohkubo, T. Mukai, and K. Hono, Plasticity and microstructure of Zr-Cu-Al bulk metallic glasses, Scr. Mater. **57**, 173 (2007).

[37] K. Wang, T. Fujita, Y. Q. Zeng, N. Nishiyama, A. Inoue, and M. W. Chen, Micromechanisms of serrated flow in a $Ni_{50}Pd_{30}P_{20}$ bulk metallic glass with a large compression plasticity, Acta Mater. **56**, 2834 (2008).

[38] V. Schmidt, H. Rösner, M. Peterlechner, G. Wilde, and P. M. Voyles, Quantitative Measurement of Density in a Shear Band of Metallic Glass Monitored along its Propagation Direction, Phys. Rev. Lett. **115**, 035501 (2015).

[39] D. Schryvers, G. S. Firstov, J. W. Seo, J. Van Humbeeck, and Yu. N. Koval, Unit cell determination in CuZr martensite by electron microscopy and X-ray diffraction, Scr. Mater. **36**, 1119 (1997).

[40] S. Plimpton, Fast parallel algorithms for short-range molecular dynamics, J. Comput. Phys. **117**, 1 (1995); http://lammps.sandia.gov/.

[41] M. I. Mendelev, M. J. Kramer, R. T. Ott, D. J. Sordelet, D. Yagodin, and P. Popel, Development of suitable interatomic potentials for simulation of liquid and amorphous Cu-Zr alloys, Philos. Mag. **89**, 967 (2009).

[42] S. Pauly, J. Das, C. Duhamel, and J. Eckert, Martensite formation in a ductile $Cu_{47.5}Zr_{47.5}Al_5$ bulk metallic glass composite, Adv. Eng. Mater. **9**, 487 (2007).

[43] Y. F. Sun, B. C. Wei, Y. R. Wang, W. H. Li, T. L. Cheung, and C. H. Shek, Plasticity-improved Zr-Cu-Al bulk metallic glass matrix composites containing martensite phase, Appl. Phys. Lett. **87**, 051905 (2005).

[44] J. Das, S. Pauly, C. Duhamel, B. C. Wei, and J. Eckert, Microstructure and mechanical properties of slowly cooled $Cu_{47.5}Zr_{47.5}Al_5$, J. Mater. Res. **22**, 326 (2007).

[45] F. Jiang, D. H. Zhang, L. C. Zhang, Z. B. Zhang, L. He, J. Sun, and Z. F. Zhang, Microstructure evolution and mechanical properties of $Cu_{46}Zr_{47}Al_7$ bulk metallic glass composite containing CuZr crystallizing phases, Mater. Sci. Eng. A **467**, 139 (2007).

[46] F. Shimizu, S. Ogata, and J. Li, Theory of shear banding in metallic glasses and molecular dynamics calculations, Mater. Trans., JIM **48**, 2923 (2007).

[47] A. Stukowski, Visualization and analysis of atomistic simulation data with OVITO—The Open Visualization Tool, Model. Simul. Mater. Sci. Eng. **18**, 015012 (2010); http://ovito.org.

[48] A. Stukowski, Structure identification methods for atomistic simulations of crystalline materials, Model. Simul. Mater. Sci. Eng. **20**, 045021 (2012).

[49] A. H. Cottrell, *Dislocations and Plastic Flow in Crystals* (Clarendon, Oxford, 1953).

[50] J. P. Hirth and J. Lothe, *Theory of Dislocations*, 2nd ed. (Krieger, Malabar, FL, 1982).

[51] G. Gottstein, *Physical Foundations of Materials Science* (Springer, New York, 2004).

[52] G. Wang, S. Pauly, S. Gorantla, N. Mattern, and J. Eckert, Plastic flow of a $Cu_{50}Zr_{45}Ti_5$ bulk metallic glass composite, J. Mater. Sci. Technol. (Sofia) **30**, 609 (2014).

[53] L. Ward, A. Agrawal, K. M. Flores, and W. Windl, Rapid production of accurate embedded-atom method potentials for metal alloys, arXiv:1209.0619.

[54] X. W. Zhou, R. A. Johnson, and H. N. G. Wadley, Misfit-energy-increasing dislocations in vapor-deposited CoFe/NiFe multilayers, Phys. Rev. B **69**, 144113 (2004).

[55] Y. Ritter and K. Albe, Thermal annealing of shear bands in deformed metallic glasses: Recovery mechanisms in $Cu_{64}Zr_{36}$ studied by molecular dynamics simulations, Acta Mater. **59**, 7082 (2011).

[56] C. N. Kuo, J. C. Huang, J. B. Li, J. S. C. Jang, C. H. Lin, and T. G. Nieh, Effects of B2 precipitate size on transformation-induced plasticity of Cu-Zr-Al glassy alloys, J. Alloys Compd. **590**, 453 (2014).

[57] R. J. Hebert, J. H. Perepezko, H. Rösner, and G. Wilde, Dislocation formation during deformation-induced synthesis of nanocrystals in amorphous and partially crystalline amorphous $Al_{88}Y_7Fe_5$ alloy, Scr. Mater. **54**, 25 (2006).

[58] S. Ogata, J. Li, and S. Yip, Ideal pure shear strength of aluminum and copper, Science **298**, 807 (2002).